

An expanding ring of the hypercompact HII region W49N:A2

Ryosuke Miyawaki¹, Masahiko Hayashi^{2,3}, and Tetsuo Hasegawa²

¹College of Arts and Sciences, J.F. Oberlin University, Machida, Tokyo 194-0294, Japan

²National Astronomical Observatory of Japan, 2-21-1 Osawa, Mitaka, Tokyo 181-8588, Japan

³JSPS Bonn Office, Ahrstr. 58, 53175 Bonn, Germany

*E-mail: miyawaki@obirin.ac.jp

Received (03–Aug–2022); Accepted (05–Dec–2022)

Abstract

We present 250 GHz continuum and H29 α line data toward W49N:A2, a hypercompact HII region ionized by an O9 star. The data obtained with ALMA at a resolution of $\sim 0.''05$ (600 au) confirmed the presence of an ionized ring with a radius of ~ 700 au inclined by $\sim 50^\circ$ (0° for pole-on). It has a width of ~ 1000 au and is relatively flat with a scale height of less than several hundred au. The tilted ring, or the apparent ellipse, has a prominent velocity difference between its NW and SE ridges along the minor axis, suggesting that it is expanding in the equatorial plane at a velocity of 13.2 km s^{-1} . The ring also shows a hint of rotation at 2.7 km s^{-1} , which is significantly (2.5σ) smaller than the Kepler velocity of 5.2 km s^{-1} at its radius around the $20 M_\odot$ star. This can be interpreted that the ring gas has been transported from the radius of ~ 170 au by conserving its original specific angular momentum that it had there. The ionized ring may thus be a remnant of the accretion disk that fed the O9 star, whose radiation or magnetic activities became so strong that the disk accretion was reversed due to the intense thermal or magneto-hydrodynamic pressure around the star. The data has revealed a rare example of how a massive star terminates its accretion at the end of its formation, transforming a hypercompact HII region into an ultracompact HII region.

Key words: ISM: jets and outflows, HII regions—radio lines: ISM: individual (W49N), stars: massive, formation

1 Introduction

Hypercompact HII (HCHII) regions are characterized by their small sizes ($< 0.05 \text{ pc}$ or $10,000 \text{ au}$), high electron densities ($n_e > 10^6 \text{ cm}^{-3}$), large emission measures ($> 10^8 \text{ pc cm}^{-6}$), and broad radio recombination line widths ($\Delta V > 40 \text{ km s}^{-1}$) (Sewilo et al. 2004; Kurtz 2005; Murphy et al. 2010). They are considered to precede the phase of ultracompact HII (UCHII) regions in massive star formation.

Photoevaporating accretion disk models may explain the characteristics of HCHII regions (Hollenbach et al. 1994; Lizano et al. 1996; Keto 2007), in which inevitable outflows may be responsible for the broad radio recombination lines (e.g., Tanaka et al. 2016). Alternatively, the broad line width may also be explained by the pressure broadening caused by the

high-density ionized gas in HCHII regions (e.g., Brocklehurst & Seaton 1972; Kurtz 2005). Numerical calculations show that a small quasi-spherical HII region first forms within the accretion flow (Keto 2007). The initial HII region is gravitationally trapped within the Bondi-Parker radius, while the accretion may proceed through the HII region (Keto 2002). As the ionizing flux increases, the HII region expands driven by the ionized gas pressure, transitioning to an ionized bipolar outflow, and eventually, as the outflow opening angle increases, the accretion flow is confined to a thin disk. The photoionization of the bipolar low-density cavities pushes mass from high latitudes toward the disk. This feedback yields an increase in disk mass and hence stellar accretion rate in the last stage of massive star formation (Kuiper & Hosokawa 2018).

W49N:A is one of the UCHII regions cataloged by De Pree

et al. (1997) in their 8.3 GHz map. Higher resolution observations at 45 GHz have resolved it into two sources A1 and A2 (De Pree et al. 2000), with A2 showing a distinct ring located at the center of the oppositely directed, edge-brightened bipolar lobes of ionized gas (De Pree et al. 2020). W49N:A2 is ionized by a Lyman continuum photon luminosity equivalent to an O9 ZAMS star and has the total ionized gas mass of $0.12 M_{\odot}$ (De Pree et al. 2020). In this paper, we present the 250 GHz continuum and H29 α line data for W49N:A2 and examine its kinematics. We assume the distance to W49N to be $11.11^{+0.79}_{-0.69}$ kpc (Zhang et al. 2013) throughout this paper.

2 ALMA archival data

We used Atacama Large Millimeter/submillimeter Array (ALMA) archival data (#2018.1.00520.S; PI D. Wilner) for the study of protostars in W49N. The observations were performed from July 2019 to September 2019 using 43–48 12-m antennas. The shortest and longest baselines for the 12-m antennas were 38.4 m and 3637.7 m, respectively. Flux, bandpass, pointing, and phase calibrations were carried out with J1905+0952, J1907+0907, and J1908+1201.

Four spectral windows (240.76–242.63 GHz, 242.61–244.49 GHz, 255.86–257.74 GHz, and 257.70–259.57 GHz), each covering a 2 GHz bandwidth, were set up to observe the target source W49N. Image analysis was done using the CASA software (The CASA Team et al. 2022). We separated the continuum and line emissions by fitting a linear baseline to line free channels of each spectral window using the ‘uvcontsub’ task of CASA. The continuum data at the effective frequency of 250 GHz was then made by averaging the line-free intensities of all four windows.

For the H29 α line data, we set up a data cube with a spectral resolution of 2 km s^{-1} . Although the frequency resolution (channel width) was 1128.91 kHz ($\sim 1.31 \text{ km s}^{-1}$), there was variation in frequency to channel relation between datasets obtained on different days. We thus proportionally distributed the flux received in an original spectral channel into the nearest 2 km s^{-1} bins by setting the width parameter of the ‘tclean’ task to be 2 km s^{-1} to compensate for the variation. We analyzed three sets of data 3.1 hours long in total, but the second set showed a large noise level probably due to errors in the calibration process, and was not used.

The phase center was $\alpha(\text{ICRS}) = 19^{\text{h}}10^{\text{m}}13^{\text{s}}.300$ and $\delta(\text{ICRS}) = 09^{\circ}06'14''.00$ with a primary beam field of view (HPBW) of $23''.3$. We set the parameters of the ‘tclean’ task as `weighting='briggs'` and `robust='0.5'`. This setting creates a PSF that smoothly varies between natural and uniform weighting based on the signal-to-noise ratio of the measurements and a tunable parameter that defines the noise threshold. The synthesized beam size of the continuum image was $0''.046 \times$

$0''.032$ (PA= 70.3°) at the effective frequency of 250 GHz, and that of the H29 α recombination line image was $0''.052 \times 0''.033$ (PA= 58.0°) at its frequency of 256 GHz. The resultant noise levels were $0.7 \text{ mJy beam}^{-1}$ and $2.0 \text{ mJy beam}^{-1}$ for the continuum and line maps, respectively.

3 Results and discussion

3.1 Continuum and H29 α Rings

Figure 1 shows the 250 GHz continuum image of W49N:A2, with A1 also seen at its $\sim 0''.4$ north. A2 exhibits an extended emission elongated from the NE to SW with a central dip surrounded by a ridge of elliptical emission. This feature was first noted by De Pree et al. (2000) in their 45 GHz continuum map, which is shown by contours in Figure 1 for comparison.¹ This kind of annular morphology is relatively common in UCHII regions and is interpreted as a ring or a shell, which may be distinguishable from the observed contrast ratio between the flux density of the shell peak and that of the cavity (Turner & Matthews 1984). For the 45 GHz image of W49N:A2, the ratio is *inconsistent* with a shell morphology, and the observed elliptical structure is interpreted as a ring or a flattened disk with a central gap of diameter $\sim 0''.08$ ($\sim 880 \text{ au}$) (De Pree et al. 2000, 2020). The major axis of the ellipse is perpendicular to the axis of the ionized bipolar outflow seen as an edge-brightened double-lobed structure in the 8.3 GHz maps (De Pree et al. 1997, 2020), which also suggests that the observed elliptical structure is a tilted equatorial ring perpendicular to the outflow. We, therefore, assume in this paper that the 250 GHz elliptical emission represents a tilted ring, which is intrinsically circular on the equatorial plane of the star. The ring is supposed to be geometrically and kinematically symmetric with respect to the polar axis of the star (rotational symmetry) and its equatorial plane (plane symmetry).

Table 1 lists the observed parameters of W49N:A2 derived from the 2D Gaussian fitting tool of CASA. The total flux density of A2 at 250 GHz is 1.11 Jy, which is compared with its 45 GHz flux density of 0.47 Jy to give a spectral index $\alpha = 0.5$ ($F_{\nu} \propto \nu^{\alpha}$). Preliminary measurements using additional archival data resulted in the flux densities of $1.3 \pm 0.3 \text{ Jy}$, $2.7 \pm 0.2 \text{ Jy}$, $1.3 \pm 0.2 \text{ Jy}$, and $0.59 \pm 0.09 \text{ Jy}$ at 100 GHz, 230 GHz, 360 GHz, and 450 GHz, respectively, including both A2 and A1.² If we use all these data points, we obtain $\alpha = 0.4 \pm 0.7$, indicating that

¹ The 45 GHz continuum map is shifted by $(\Delta\alpha, \Delta\delta) = (-0''.019, -0''.065)$ from its original coordinates so that the peak position of A1 coincides with that of the 250 GHz map to compensate the unknown positional displacement described by Rodríguez et al. (2020). We also applied the task ‘phaseshift’ to CLEAN the data but did not obtain any different results.

² ALMA archival data: 100GHz (#2018.1.00589.S PI: R. Galván-Madrid), 230GHz (#2016.1.00620.S PI: A. Ginsburg), 360GHz (#2015.1.01535.S PI: B. R. Alejandro and #2017.1.00318.S PI: R. Galván-Madrid), 450GHz (#2017.1.01499.S PI: F. Xiaoting)

Table 1. Observed parameters

	250 GHz continuum	H29 α line	45 GHz continuum*
Center Position			
α (ICRS) 19 ^h 10 ^m +	12 ^s :8921 \pm 0 ^s :0003	12 ^s :8927 \pm 0 ^s :0005	12 ^s :8929 \pm 0 ^s :0001
δ (ICRS) 09 ^o 06'+	11 ^{''} :756 \pm 0 ^{''} :004	11 ^{''} :781 \pm 0 ^{''} :008	11 ^{''} :837 \pm 0 ^{''} :002
Beam Size (position angle)	0 ^{''} :046 \times 0 ^{''} :032 (70.3 ^o)	0 ^{''} :052 \times 0 ^{''} :033 (61.5 ^o)	0 ^{''} :055 \times 0 ^{''} :044 (8.6 ^o)
Image Component Size [†]			
Major axis FWHM	400 \pm 20 (mas)	510 \pm 30 (mas)	270 \pm 6 (mas)
Minor axis FWHM	220 \pm 10 (mas)	310 \pm 20 (mas)	182 \pm 4 (mas)
Position Angle	58 ^o \pm 2 ^o	40 ^o \pm 4 ^o	53 ^o \pm 3 ^o
Inclination Angle	57 ^o \pm 2 ^o	53 ^o \pm 3 ^o	48 ^o \pm 2 ^o
Peak Brightness	18.3 \pm 0.1 (mJy beam ⁻¹)	1.48 \pm 0.07 (Jy beam ⁻¹ km s ⁻¹)	22.2 \pm 0.5 (mJy beam ⁻¹)
Total Flux Density	1.11 \pm 0.03 (Jy)	152 \pm 7 (Jy km s ⁻¹)	0.47 \pm 0.01 (Jy)
Ring Size [‡]			
Major Axis (PA=55 ^o)	124 \pm 4 (mas)	116 \pm 10 (mas)	117 \pm 5 (mas)
Minor Axis (PA=145 ^o)	79 \pm 1 (mas)	82 \pm 3 (mas)	96 \pm 4 (mas)
Inclination Angle	50 ^o \pm 2 ^o	45 ^o \pm 6 ^o	35 ^o \pm 5 ^o
Ring Width ^{†‡}			
Major Axis FWHM (2 a)	90 \pm 12 (mas)	103 \pm 41 (mas)	84 \pm 38 (mas)
Minor Axis FWHM (2 β)	54 \pm 9 (mas)	62 \pm 11 (mas)	78 \pm 39 (mas)
cos ⁻¹ (β/a)	53 ^o \pm 9 ^o	53 ^o \pm 19 ^o	22 ^o \pm 97 ^o

*De Pree et al. (2000, 2020). The center position shows their original coordinates (see footnote 1).

[†]Beam deconvolved FWHM

[‡]Measured by fitting a double Gaussian to each spatial profile.

the source has a flat or slowly rising spectrum. The flux density distribution does not show any steeply ($\alpha > 2$) rising tendency toward submillimeter wavelengths, suggesting a negligible contribution from thermal dust emission at these frequencies. We examined any molecular line emission directly toward the A2 nebulecity in the current archive data, finding no molecular lines significantly detected within 200 mas in radius, inside which the ionized ring is located. In particular, the lines of CH₃CN ($J_K = 14_K - 13_K$), which would be a dominant molecular emission in the band if molecular gas existed, show very little ($< 3\sigma$) emission there. In fact, the CH₃CN emission was detected around A2 at radii larger than 200 mas, corresponding to the outside of the main ionized nebula A2. This tendency is the same for emissions from other molecular lines such as ¹³CO or SO. In other words, there is a hole of molecular emission toward A2, suggesting that no neutral disk is associated with the ionized ring inside the emission nebula A2.

The 250 GHz emission has the major and minor axis lengths of 400 mas \times 220 mas (deconvolved FWHM), respectively, corresponding to 4400 au \times 2400 au, with a major axis position angle of 58^o. This gives an inclination angle of 57^o \pm 2^o (0^o for pole-on) if a geometrically thin circular structure is assumed. The distance between the two ridges of the ring is 124 \pm 4 mas along the major axis, corresponding to 690 au, and 79 \pm 1 mas

along the minor axis, when a double gaussian fit is applied to the spatial profiles. The minor to major axis ratio of the ring suggests an inclination of 50^o \pm 2^o if we assume that the ring is intrinsically circular when viewed pole-on.

Figure 2 shows the moment 0 map of the H29 α emission integrated over the velocity range from -20 to 60 km s⁻¹ superposed on the 250 GHz continuum contours. The line emission follows the continuum map well, showing the elliptical ring of 116 mas \times 82 mas, which are the distances between the ridges along the major (PA=55^o) and minor (PA=145^o) axes, respectively. The ring's axis lengths are consistent between the 250 GHz and H29 α data within the errors. We can thus naturally assume that the H29 α emission represents the same ring as the 250 GHz continuum. The minor to major axis ratio of the H29 α ring gives the inclination angle of 45^o \pm 6^o.

Table 1 also lists the beam deconvolved FWHM widths of the ring along the major and minor axes. The widths along the ring's major axis, corresponding to its radial width on the equatorial plane, are 90 mas (1000 au) and 100 mas (1100 au) for the 250 GHz and H29 α , respectively. They are consistently larger than the widths of 54 mas and 60 mas along the minor axis for the 250 GHz and H29 α rings, respectively. This means that the ring has a smaller thickness than its radial width as we will discuss below. This tendency was not confirmed for the 45 GHz

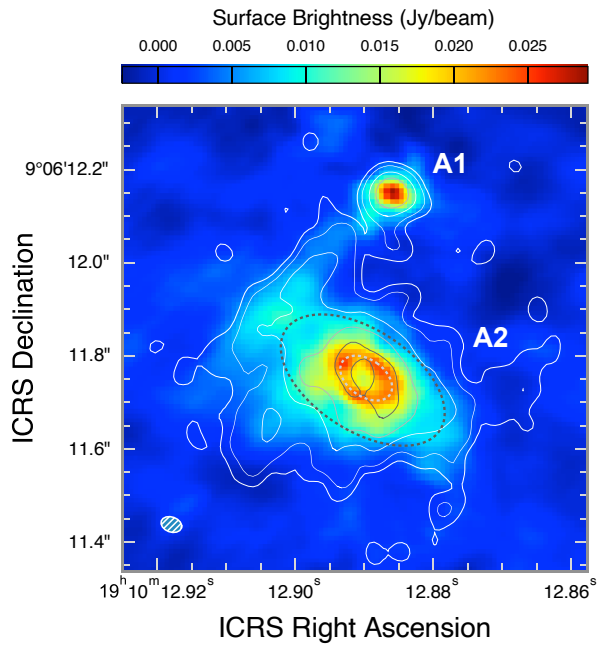


Fig. 1. The 250 GHz continuum map superposed on the contours of the 45 GHz continuum emission (De Pree et al. 2000) at 1, 2, 5, 10, and 20 mJy beam⁻¹. The two dotted ellipses show the ring (white) and the FWHM size of the entire emission nebula (black).

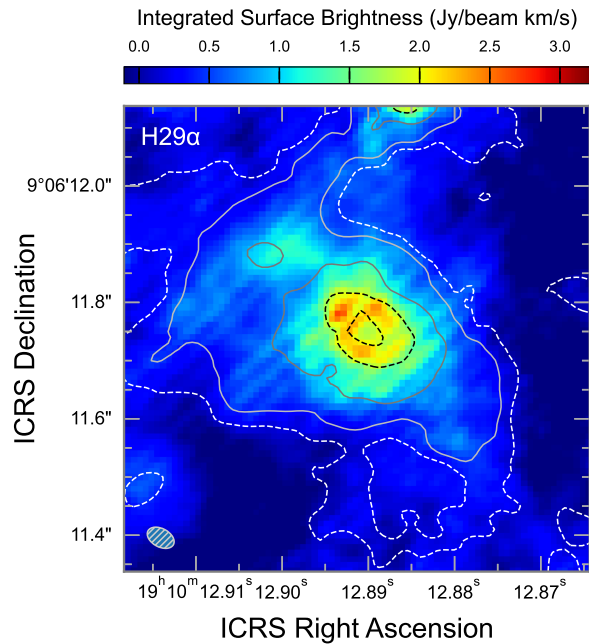


Fig. 2. Integrated intensity (moment 0) map of the H29 α emission superposed on the 250 GHz continuum contours at 1, 2, 5 and 10 % of 194 mJy beam⁻¹. The integration range is from $V_{\text{LSR}} = -20$ to 60 km s⁻¹.

ring. This is because the 45 GHz ring does not show a clear elliptical shape (see Fig. 2 (i) of De Pree et al. 2000), and the double Gaussian fit to its spatial profiles along the major and minor axes gives large errors for the ring widths. We will thus use only the 250 GHz and H29 α data for the following discussion about the scale height.

To estimate the scale height of the ring, we assume a simple model that the ring has an elliptical cross-section with the semi-axis lengths of a and b along the ring's equatorial plane and polar axis, respectively. The configuration is shown in Figure 3. The ellipse on the left shows the tilted ring projected on the plane of the sky, while the ellipse on the right is a cross-section of the ring cut along the plane defined by the ring's polar and radial axes. Under this model, the value $2a$ represents the non-projected radial width of the ring and $2b$ stands for its thickness, i.e., two times the scale height. The value 2β is the apparent width of the projected ring along its minor axis.

The ring width $2a$ can be directly measured by the width of the projected ring along its major axis, while the value 2β can be obtained from the width of the projected ring along its minor axis. The scale height b is then estimated from the values of a and β using the geometrical relation $\beta^2 = a^2 \cos^2 i + b^2 \sin^2 i$, where i is the inclination angle of the ring ($i = 0^\circ$ for pole-on). If, for example, the ring cross section was circular, i.e., $a = b$, we would obtain the trivial result $\beta = a$. If the ring was flat, i.e., $b = 0$, we would obtain another trivial result $\beta = a \cos i$.

For the 250 GHz and H29 α data in Table 1, the ring widths a and β are relatively well defined. The values of $\cos^{-1}(\beta/a)$ are consistent with the ring inclination angle of 50° and 45° , respectively, within the errors. This means that the value $b = 0$ is consistent with the observations, suggesting that the ring is relatively flat having a small scale height. We estimate a 2σ upper limit to the scale height b by taking 2σ larger and smaller values for β and a , respectively. The results are $b < 410$ au and $b < 690$ au for the 250 GHz and H29 α rings, respectively. As expected, the ring's scale height is smaller than its radial widths of ~ 1000 au. It is also significantly smaller than the pressure scale height of ~ 1700 au of an ionized gas disk of 10000 K around a 20 M_\odot star at a radius of 690 au, implying that the ring is not a static structure and is being evaporated by the ionizing radiation from the central star.

3.2 Velocity structure of the ring

Figure 4 shows the velocity channel maps of the H29 α line, together with a moment 1 (mean velocity) map on the bottom right panel. It demonstrates a clear velocity shift along the minor axis of the elliptical ring. The NW half of the ring is bright at the radial velocities less than 0 km s⁻¹, while the SE part is bright at velocities larger than 30 km s⁻¹. Under our assumption that the ring is intrinsically circular and symmetric with respect to its polar axis and equatorial plane, the line of sight velocity toward the minor axis reflects only the radial motion of the tilted ring, but not its rotational motion (see Figure 3). Thus the observed large velocity difference between the two ridges along the minor axis means that radial motion is dominant in the ring. Whether the motion corresponds to expansion or contraction is

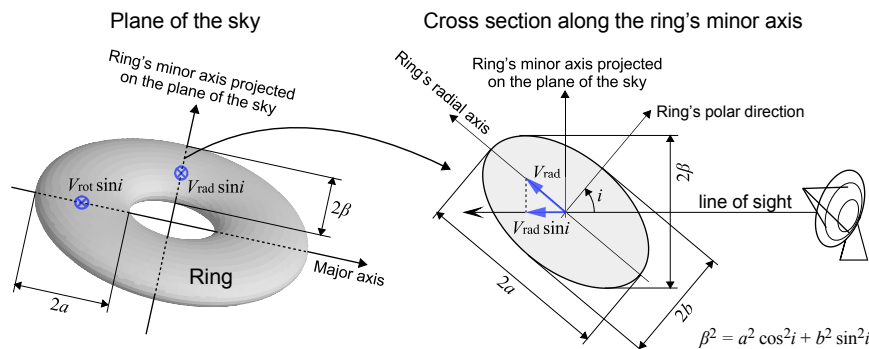


Fig. 3. A ring model with an elliptical cross-section. The observed width 2β of the ring along the minor axis on the plane of the sky is related to the elliptical semi-axis lengths a and b as $\beta^2 = a^2 \cos^2 i + b^2 \sin^2 i$, where i is the inclination of the ring ($i = 0$ for pole-on). If the ring has a radial (expansion or contraction) velocity V_{rad} and a rotational velocity V_{rot} along its equatorial plane, the line of sight velocities toward the major and minor axes are $\pm V_{\text{rot}} \sin i$ and $\pm V_{\text{rad}} \sin i$, respectively.

not straightforward, and will be discussed in the next section (§3.3).

At $V_{\text{LSR}} = -10$ and 0 km s^{-1} , there is a hint that the NE side of the ring has stronger emission than the SW side. At $V_{\text{LSR}} = 40$ and 50 km s^{-1} , the emission peak is slightly shifted to the west along the southern part of the ring with respect to the minor axis of symmetry.

To examine this tendency in more detail, we show in Figure 5 the position velocity diagrams along the major and minor axes. The velocity difference across the minor axis is obvious (right panels). The PV diagrams along the strips parallel to the major axis (left panels) show convex features on the SE side, and, alternatively, concave features on the opposite NW side. Such convex/concave features in a PV diagram arise when the system has a systematic radial motion (expansion or contraction). The entire ring thus has a consistent radial motion, either expansion or contraction³

In the PV diagram at offset $0''$ along the major axis, we do not see a drastic velocity change with positions. There seems to be a subtle difference in the line of sight velocity between the NE and SW ridges of the ring, and the entire PV diagram is marginally tilted. To examine the velocity structure of the ring in more detail, we plotted in Figure 6 the variations of peak brightness, peak velocity, and FWHM velocity width of the $\text{H}29\alpha$ line along the major (left) and minor (right) axes. The values were measured by applying Gaussian fits to the line profiles on the PV diagrams.

The radial velocities along the minor axis are 26.3 km s^{-1} and 6.0 km s^{-1} at its SE ($-0'.035$) and NW ($+0'.047$) ridges,

³ This conclusion is valid even if the ring, with its center at the exciting star, is tilted with respect to the equatorial plane. Thus, if we take an assumption that the ring is, for example, on the polar plane of the star, we derive the same conclusion that the ring has a radial motion. We, however, do not take such an assumption because it is simply unphysical: we do not find any reason that the inflowing or outflowing gas forms a regular ring on a plane significantly tilted with respect to the equatorial plane of the star, breaking the rotational symmetry about the polar axis.

respectively. The apparent “smooth” velocity gradient from the SE to NW ridge is naturally attributed to a stepwise velocity difference smeared by the beam, which has an HPBW similar to the ring width. Because the velocity difference between the SE and NW ridges along the minor axis is caused either by expansion or contraction of the ring under our geometrical and kinematical assumptions, the velocity difference gives an expansion or contraction velocity of $13.2 \pm 1.0 \text{ km s}^{-1}$ at the radius of 706 au after correcting for the inclination angle, which is taken to be 50° .

The radial velocity along the major axis, which solely reflects the ring’s rotation velocity under our assumption, varies from 17.2 km s^{-1} to 21.4 km s^{-1} as the position moves from the NE peak at $-0'.073$ to the SW peak at $+0'.042$. The velocity difference corresponds to a rotation velocity of $2.7 \pm 1.0 \text{ km s}^{-1}$ at the radius of 642 au after correcting for the inclination angle.

3.3 Expanding ring of ionized gas and its implication

We have found a remarkable fact that the ionized ring of W49N:A2 has a predominant radial motion of $13.2 \pm 1.0 \text{ km s}^{-1}$, with a hint of rotation at $2.7 \pm 1.0 \text{ km s}^{-1}$, at ~ 700 au in radius. The ionizing source of A2 emits Lyman continuum photons equivalent to an O9 (ZAMS) star (De Pree et al. 2020), which should have a mass of $20 \pm 7 M_\odot$ ⁴ (Hohle, Neuhäuser, & Schutz 2010). The ionized gas mass of A2 is $0.12 M_\odot$ (De Pree et al. 2020), which, together with the absence of molecular and dust emissions toward A2, implies that the total amount of mass within the ring cannot be much larger than $20 M_\odot$.

It is impossible that this amount of mass gravitationally accelerates any gas to $\sim 13 \text{ km s}^{-1}$ at a distance of $R = 700$ au from the center of A2. We would need a total mass as large as $70 M_\odot$ if a lump of gas freely falling toward the central star obtains the three-dimensional velocity of $\sim 13 \text{ km s}^{-1}$ at the radius.

⁴ Mean and standard deviation of mass for field O9 stars with the luminosity classes I, III and V.

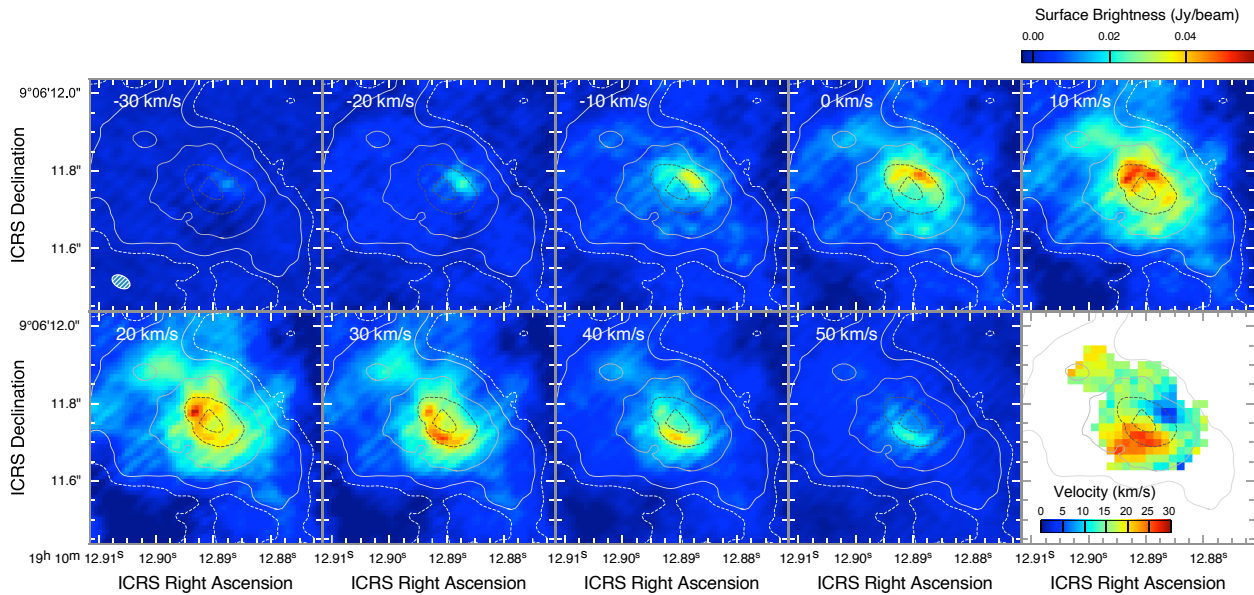


Fig. 4. Velocity channel maps of the H29 α line superposed on the 250 GHz continuum contours at 1, 2, 5 and 10 % of 194 mJy beam $^{-1}$. The bottom right panel shows a mean velocity (moment 1) map.

Alternatively, we can derive a Keplerian mass of 5.3–5.7 M_{\odot} from the inclination-corrected rotation velocity of 2.7 km s $^{-1}$ at a radius of 642–700 au. This mass is significantly smaller than the expected mass of an O9 star. We, therefore, conclude that the ring’s observed radial motion cannot be gravitational infall or contraction.

Expansion, on the other hand, is a natural cause of motion. At the beginning of HII region formation, ionized gas around a massive star is pushed outward due to the thermal pressure or magneto-hydrodynamical acceleration (Commerçon et al. 2022). A radially expanding motion perpendicular to the outflow axis has, for example, been observed toward Orion Source I (Hirota et al. 2017), where the expansion velocity of ~ 10 km s $^{-1}$ was observed above and below the disk plane that is supposed to be driving a magneto-centrifugal outflow.

The current case of A2 has a linear scale 10 times larger than the case of Source I, so we are unable to resolve the motion in the disk from that in the outflow. However, the entire ionized ring, which could be a mixture of a disk and an outflow, shows expansion with a hint of rotation, while in the case of Source I no radial motion was detected in the disk plane and rotation is dominant there. In the case of W49N:A2, the dominant motion in its equatorial plane is expansion.

The small rotation velocity of the A2 ring is consistent with its expanding motion. The observed rotation velocity at $R \sim 650$ au is 2.7 ± 1.0 km s $^{-1}$, which is significantly (2.5σ) smaller than the Kepler velocity of 5.2 km s $^{-1}$ at the radius around a 20 M_{\odot} star. It may be the case that the gas at $R \sim 650$ au has been transported from an inner radius, specifically from $R \sim 170$ au. The gas was originally in Keplerian rotation at the radius but was pushed out to the current radius by conserving its

specific angular momentum of ~ 1800 au km s $^{-1}$. Such a phenomenon may occur when the accretion through the equatorial disk becomes hampered and reversed by the intense thermal or magneto-hydrodynamical pressure caused by the central star as its luminosity increases dramatically at the end of Kelvin-Helmholtz contraction (Tanaka et al. 2016, 2017). Although we cannot exclude the possibility of a small amount of accretion through the mid-plane of the disk even at this later stage of massive star formation, we did not find any evidence of accretion around the ionizing star of A2.

The ionized gas toward A2 shows broad H29 α line widths of $\Delta V = 40$ –60 km s $^{-1}$, which may be attributed to a gas outflow with a large opening angle or to pressure broadening due to the high-density (Brocklehurst & Seaton 1972; Kurtz 2005). There is a marginal increase in line width inside the ring, seen on the upper panels of Figure 6. The outflow there may have a higher velocity because it is accelerated in a region closer to the central star, or the outflow there is preferentially directed toward the polar direction.

From these pieces of observational evidence, we conclude that the massive star ionizing the HCHII region W49N:A2 has finished its main accretion phase and is in the phase of disrupting its natal accretion disk. W49N:A2 thus provides an example of how a massive star terminates its accretion at the end of its formation. As time goes on, the ring will be fully evaporated by the stellar radiation. The ionized outflow will expand by gradually decreasing its expansion velocity, and the HCHII region will eventually become a UCHII region. Figure 7 shows a schematic drawing of the observed features, where outflow velocities are derived from the H29 α line widths deconvolved by its thermal widths at the assumed temperature of 10000 K

(De Pree et al. 1997).

4 Conclusions

We have presented ALMA archival data for 241–260 GHz continuum and H29 α recombination line observations toward the HCHII region W49N:A2 at a resolution of $\sim 0''.05$. (600 au), confirming the presence of an ionized ring of ~ 700 au in radius inclined by $\sim 50^\circ$. The tilted ring has a prominent velocity difference between its NW and SE ridges along the minor axis, suggesting that it is expanding in the equatorial plane at a velocity of 13.2 km s^{-1} .

The ring also shows a hint of rotation at 2.7 km s^{-1} , which is significantly (2.5σ) smaller than the Kepler velocity of 5.2 km s^{-1} at the ring radius around a $20 M_\odot$ star. This can be interpreted that the ring gas has been transported from the radius of ~ 170 au by conserving its original specific angular momentum that it had there. The ionized ring may thus be a remnant of the accretion disk that fed the O9 star, whose radiation or magnetic activities recently became so strong that the accretion was reversed. W49N:A2 provides a rare example of how a massive star terminates its accretion at the end of its formation and how an HCHII region transitions to a UCHII region.

Acknowledgments

ALMA is a partnership of ESO (representing its member states), NSF (USA), and NINS (Japan), together with NRC (Canada), NSC and ASIAA (Taiwan), and KASI (Republic of Korea), in cooperation with the Republic of Chile. The Joint ALMA Observatory is operated by ESO, AUI/NRAO, and NAOJ. We used the ALMA archival data #2018.1.00520.S (PI: D. Wilner), #2018.1.00589.S (PI: R. Galván-Madrid), #2016.1.00620.S (PI: A. Ginsburg), #2015.1.01535.S (PI: B. R. Alejandro), #2017.1.00318.S (PI: R. Galván-Madrid), #2017.1.01499.S (PI: F. Xiaoting).

References

Brocklehurst, M. & Searyon, M. F. 1972, MNRAS, 157, 179
 THE CASA TEAM, Bean, B., Bhatnagar, S., Castro, S., Meyer, J. D., Emonts, B., Garcia, E., Garwood, R., et al. 2022, PASP, in press
 Commerçon, B., González, M., Mignon-Risse, R., Hennebelle, P. & Vaytet, N. 2022, A&A 658, A52
 De Pree, C. G., Mehringer, D. M., & Goss, W. M. 1997, ApJ, 482, 307
 De Pree, C. G., Wilner, D. J., Goss, W. M., Welch, W. J., & McGrath, E. 2000, ApJ, 540, 308
 De Pree, C. G., et al. 2020, AJ, 160, 234
 Hirota, T., Machida, M. N., Matsushita, Y., Motogi, K., Matsumoto, N., Kim, M. K., Burns, R. A., & Honma, M. 2017, Nat. Astron., 1, 0146
 Hohle, M. M., R. Neuhäuser, & Schutz. B. F. 2010, AN, 331, 349
 Hollenbach, D., Johnstone, D., & Lizano, S. 1994, ApJ, 428, 654
 Keto E., 2002, ApJ, 580, 980
 Keto, E., 2007, ApJ, 666, 976
 Kuiper, R. & Hosokawa, T. 2018, A&Ap, 616, A101

Kurtz, S. 2005, IAUS, 227, 111
 Lizano, S., Canto, J., Garay, G., & Hollenbach, D. 1996, ApJ468, 739
 Murphy, T., Cohen, M., Ekers, R. D., Green, A. J., Wark, R. M. & Moss, V. 2010, MNRAS, 405, 1560
 Rodríguez, L. F., Galván-Madrid, R., Sanchez-Bermudez, J., & De Pree, C. G. 2020, ApJ, 890, 165
 Sewilo M., Churchwell E., Kurtz S., Goss W. M., Hofner P., 2004, ApJ, 605, 285
 Tanaka, K. E. I., Tan, J. C., & Zhang, Y. 2016, ApJ, 818, 52
 Tanaka, K. E. I., Tan, J. C., Staff, J. E., & Zhang, Y. 2017, ApJ, 849, 133
 Turner, B. E., & Matthews, H. E. 1984, ApJ, 277, 164
 Zhang, B., Reid M. J., Menten, K. M., Zheng, X. W., Brunthaler, A., Dame, T. M., & Xu, Y. 2013, ApJ, 775, 79

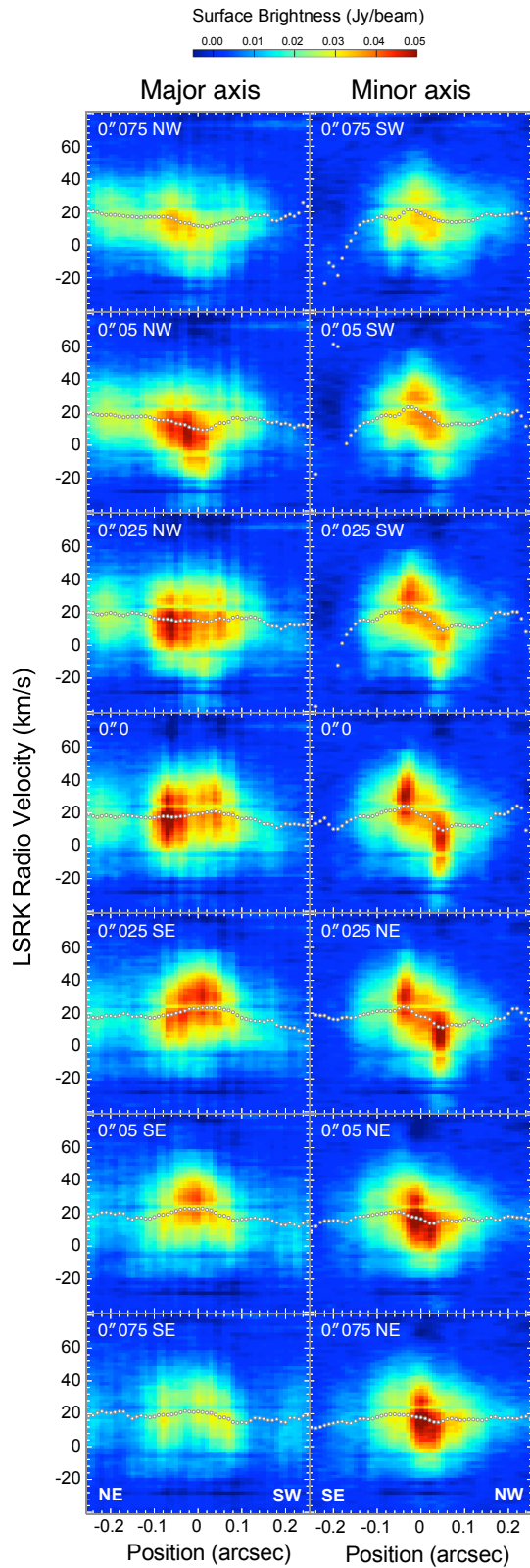


Fig. 5. Position-velocity diagrams of the $H_{29\alpha}$ line along the strips parallel to the major (PA=55°, left) and minor (PA=145°, right) axes. The brightness was averaged over three pixels (0.03) perpendicular to each strip. The offset of each strip from the major (left) or minor (right) axis is shown at the top left corner of each panel. Small circles show mean velocities.

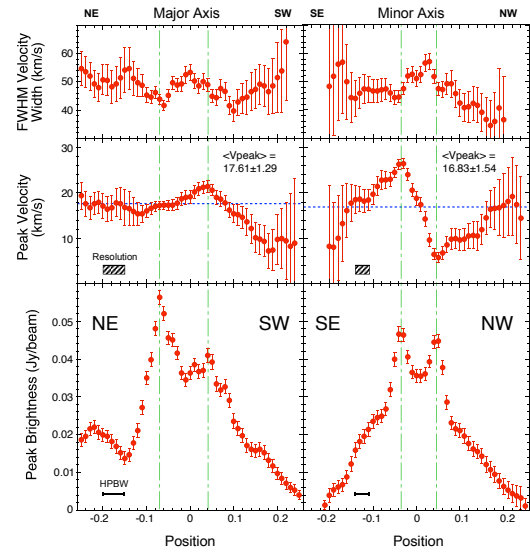


Fig. 6. Variations of peak brightness, peak velocity, and FWHM velocity width of the $H_{29\alpha}$ line along the major (left) and minor (right) axes. Data points with large errors are not plotted.

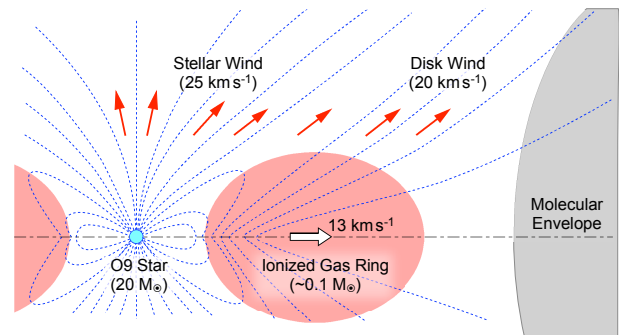


Fig. 7. A schematic drawing of W49N:A2.